MESOCALE X-RAY FLUORESCENCE (XRF) MAPPING REVEALS GROWTH

PROCESSES FOR STROMATOLITES FROM THE NSUZE GROUP

A Thesis

by

KIMBRA ROSE QUEZERGUE

Submitted to the Office of Graduate and Professional Studies of
Texas A&M University
in partial fulfillment of the requirements for the degree of

MASTER OF SCIENCE

Chair of Committee,	Michael Tice
Committee Members,	Michael Pope
	Daniel Thornton
Head of Department,	John R. Giardino

December 2014

Major Subject: Geology

ABSTRACT

Stromatolites are formed by physical, biological, and chemical processes, and combinations of specific processes produced the great variety of textures and morphologies in the geologic record. I here introduce a new technique for mesoscale chemical mapping for stromatolite interpretation. In particular, I use x-ray fluorescence microscopy (µXRF) to identify spatial associations between various elements ("fluorescence microfacies") to infer the physical, biological, and chemical processes that produced the observed compositional distributions.

As a test case, elemental distributions from µXRF scans of stromatolites from the Nsuze Group (2.98 Ga) were analyzed to develop a fluorescence microfacies growth model. There are six major fluorescence microfacies: laminated dolostone, laminated chert, clotted dolostone and chert, stromatolite clast breccia, and cavity fill. Laminated dolostone is composed of microlaminated ferroan dolomite with isolated quartz, rutile, zircon, and unidentified Fe-rich grains. Individual dolomitic laminae contain syndepositional slumps, faults, or current structures. These laminae were likely formed primarily by trapping and binding microbial mats that precipitated carbonate mud at a shallow depth below the mat surface. Laminated chert is composed of microquartz with minor fine-grained phyllosilicates, heavy minerals, and rare sand-sized K-rich grains. Pinnacle structures, roll-ups, and oversteepened laminations suggest that this fluorescence facies was produced by the secondary silicification of microbial mats. The clotted dolostone and chert fluorescence microfacies are composed of intergrown chert and dolomite, which may appear as cryptically laminated clots. It forms high-relief cauliform mounds and had high original

porosity that was frequently filled with intergrown chert and Mn-rich dolomitic cavity fill. Stromatolite clast breccias are matrix-supported breccias containing a mixture of stromatolitic clasts and heavy mineral grains. This facies was likely formed as lag deposits filling erosional scours and interstromatolite spaces. Cavities in the clotted dolostone and chert and stromatolite clast breccia fluorescence microfacies were filled by microquartz, Mn-rich dolomite, and partially dolomitized calcite (cavity fill fluorescence microfacies).

DEDICATION

To Mom and Dad

ACKNOWLEDGEMENTS

I would like to express my gratitude to my committee chair, Dr. Mike Tice and my committee members, Dr. Mike Pope, and Dr. Dan Thornton for their patience, motivation, insightful comments, and support throughout the course of this research.

Thanks goes to my Team Tice lab mates, friends, and colleagues for the stimulating discussions, for the sleepless nights, help with homework and research questions and for all the fun over the last two years. A special thanks to Amanda Poalomo, without her tireless work of XRF scanning, this research would not have been possible. Also, thanks to the faculty and staff of the Geology and Geophysics department for their help and support during my time at Texas A&M University.

Finally, thanks to my mother and father for their continued encouragement throughout my life and especially during this time.

TABLE OF CONTENTS

LIST OF FIGURES

1. BACKGROUND AND INTRODUCTION

1.1 Background

Stromatolites form one of the most important records of microbial mat communities' activities throughout geologic time, starting in the Archean. Stromatolites are some of the most studied biosignatures on Earth. For the purposes of this study, a stromatolite is an attached, laminated, lithified sedimentary growth structure, accretionary away from a point or limited surface of initiation (Kalkowsky, 1908; Grotzinger and Knoll, 1999; Tice et al., 2011) Microbial mats are comprised of surface-attached microorganisms, together with their physical substrates (Riding, 2011; Tice et al., 2011). Growth processes of microbial mat communities can be important to the formation of stromatolites. The processes that control stromatolite growth are physical, chemical, and biological (Hofmann, 1972). Physical processes involve deposition, sorting, and current re-working of sediment with the microbial mat. The growth and metabolic reactions of the microbial mat are biological processes. Chemical processes, precipitation and dissolution of carbonate are promoted and inhibited by the biological processes in the microbial mat. Combinations of these processes lead to the eventual formation of stromatolites (Riding, 1991; Grotzinger and Knoll, 1999; Hofman et al., 1999; Allwood, et al., 2009; Riding, 2011; Tice et al., 2011; Bosak, et al. 2013a; Bosak, et al. 2013b).

Trapping and binding of sediment commonly produces the irregular laminated textures in stromatolites (Grotzinger and Knoll, 1999). As filamentous microorganisms start to entangle with each other and microbial mats start to form, the stability and

1

strength of the mat will increase. When the mat is stable and the hydraulic strength of the water current cannot erode the mat, the mat will trap incoming sediment (Martin-Algarra and Sanchez-Navas, 1995; Grotzinger and Knoll, 1999; Riding, 2000; Tice et al., 2011; Bosak et al., 2013b). The communities' collective extracellular polymeric substances (EPS) can enhance the trapping process (Kawaguchi and Decho, 2000). EPS are polymers produced by the microbe that are sticky and allow for incoming sediment to become trapped in the microbial mat (Riding, 1991; Tice et al., 2011). The binding process of trapping and binding occurs when the microbes grow over or die and cover a layer of trapped sediment as the microbes search for light and nutrients. The trapped sediment becomes part of the mat and the trapping and binding process repeats (Gebelein, 1969). Trapped sediments commonly are siliclastic grains or pelagic carbonate grains (Martin-Algarra and Sanchez-Navas, 1995). Mats selectively trap fine grain sediments, such as micrite and heavy minerals, because their cohesive strength usually is insufficient to trap coarser grained sediment (Riding, 2000). However coarser grained sediment can be trapped if microbial mat strength and stability are sufficient enough that the mat will not be destroyed (Riding, 2000).

Precipitation of carbonate is a critical chemical process because early lithification is important to the formation and preservation of stromatolites (Ginsburg, 1991; Riding, 2000; Bosak, et al., 2013a). Precipitation and dissolution, although chemical processes, also commonly are controlled or induced by biological processes of the microbial mat community. There are different types of precipitation: 1) biomineralization that occurs during the life of the microbes, within their microbial cells (Weiner and Dove, 2003),

and 2) organominerialization when precipitation occurs due to interactions with microbial cells, but the precipitation occurs outside the microbial cells (Trichet and Defarge, 1995). Although different, they each typically result in the precipitation of $CaCO_3$. Commonly, for $CaCO_3$ precipitation to occur, microbial processes such as photosynthesis or sulfate reduction add metabolic products (HCO_3^- or OH^-) to the environment, increasing alkalinity and promoting $CaCO_3$ precipitation (Pentecost and Riding, 1986). EPS production or degradation can also increase the alkalinity and either inhibit or promote $CaCO_3$ precipitation, depending on the environmental conditions (Maliva and Siever, 1988; Riding, 2000; Dupraz et al., 2013).

Biological processes influence the preservation and formation of the layered structure of growing microbial mats. Microbes require energy and nutrients. Variations in those requirements result in a layered microbial mat. The layer closest to the surface is today commonly comprised of organisms that perform oxygenic photosynthesis, typically cyanobacteria, diatoms, and algae, followed by a pinkish layer and then a green layer of anoxygenic photosynthetic microbes, and then a deep layer of anaerobic heterotrophic organisms dominated by sulfate reducers (Riding, 2000; Dupraz et al., 2013). This microbial structure applies to modern mats growing in an aerobic, sulfate-rich environment; however, microbial mat structures were most likely different in the Archean, when oxygen and sulfur levels in the atmosphere were different (Olsen, 2006). The metabolic processes of these microbes and the environmental conditions outside the mat each play a role in determining the part of the mat that is cemented and preserved. Preservation often is controlled by the microbial mat layer that promotes carbonate

precipitation, unless precipitation is driven by environmental forcing. If carbonate precipitation is driven by photosynthesis, then the upper layer of mat will be preserved and lower layers may be only poorly developed. If the decay of organic matter promotes carbonate precipitation, then the lower layer of the microbial mat will be preserved.

Stromatolites have been an important geological feature since the Precambrian, when their abundances and diversity were very high (Riding, 2006). Stromatolites produce a wide variety of morphologies and textures. Common morphologies are domes, columns, branches, and clotted structures. Common textures are fine and coarsed grained lamination, sparry crust, peloid laminated, and clotted (Allwood et al., 2009; Riding, 2011). The combination of features led to the diversity of stromatolites. However at the end of the Proterozoic stromatolite abundance and diversity declined, possibly because of increased grazing and bioturbation by metazoans (Riding, 2006), a decrease in carbonate saturation of the seawater (Gattuso et al., 1998; Grotzinger and Knoll, 1999) or both. In the Phanerozoic, although there were spikes in the abundances of microbial carbonate, especially after the Late Devonian and end Permian extinctions, they never reached the abundance or diversity of the Precambrian (Riding, 2006).

1.2 Introduction

One of the missions of the Mars 2020 Rover will be to search for microbial biosignatures. To assist in this search the Mars Rover will be equipped with an X-ray fluorescence spectrometer, the Planetary Instrument for X-Ray Lithochemistry (PIXL) capable of highly spatially resolved elemental analyses (Wade, et al., 2013). PIXL will use X-ray fluorescence (XRF) to determine *in situ* elemental compositions and the

spatial distributions of elements at as little as 100 μm resolution. XRF is a non-destructive technique to measure and map elemental composition of samples. The XRF instrument bombards the sample with X-rays causing atoms to emit fluorescent X-rays. By measuring the energy and fluorescence of the fluorescent photons, the instrument can identify and quantify different elements in the sample. The result of the XRF scan is an elemental map that shows the location and quantity of elements in the sample.

PIXL will search for fine-scale characteristics that could be evidence of microbial life on Mars (Webster, 2014). Microbial biosignatures are measurable trace evidence for microbial presence and processes. The different types of trace evidence were divided into three categories by Cady, 2003. The first category of evidence is whole or partially fossilized of microbial cells. The second is chemical biomarker compounds, organic molecules, and isotope data. The final category is biofabrics or sedimentary structures resulting from microbial mat processes. Thus, understanding the relationships between microbial textures, associated compositional variations, and the processes that produce them on Earth, will be critical to interpreting similar PIXL data from Mars.

Stromatolites are formed by the interaction of various physical, biological, and chemical processes (Hofmann, 1972). Different combinations of those processes produced a wide variety of stromatolite textures and morphologies. Stromatolite growth can be linked to the biology of microbial mat communities and the physical and chemical properties of the environments where the stromatolites formed (Bosak et al., 2013b).

To study the role of different biological, physical, and chemical processes in the production of stromatolites and their effects on elemental distributions, I analyzed cut slabs of stromatolitic dolostone from the Nsuze Group (2.9 Ga) in South Africa. These stromatolites are important because their morphologies and textures are well-preserved compared to other Archean stromatolites (Beukes and Lowe, 1989; Hicks et al., 2011). They are also some of the oldest stromatolites with morphological and textural diversity similar to stromatolites of the Proterozoic, Phanerozoic, and the modern (Lowe and Tice, 2007). Stromatolites formed before 3.0 Ga were usually small and poorly developed when compared to the large, morphologically and texturally varied stromatolites that formed post 3.0 Ga. It is still unclear whether this change was due to changing environmental conditions, the evolution of new stromatolite-constructing microorganisms, or qualitative changes in the community processes leading to stromatolite growth (Tice et al., 2011).

This study uses Nsuze Group samples as a test case for mesoscale chemical mapping (μXRF) in stromatolite interpretation. Elemental compositions and spatial distributions are related to early sedimentary features of the rock in "fluorescence microfacies" and used to infer growth processes. A growth and morphogenesis model for an Nsuze stromatolite is ultimately derived from the distribution of different fluorescence microfacies.

2. GEOLOGICAL BACKGROUND

The 2.9 Ga Nsuze Group was deposited nonconformably on basement granitoid rocks and is the basal unit of the 2.98 Ga to 2.87 Ga Pongola Supergroup, located in South Africa and Swaziland. Major lithologies are volcanic and siliciclastic rocks that were deposited in an intracratonic basin and experienced burial to greenschist facies metamorphism. The Nsuze Group is sub-divided into three units: the lower fluvial feldspathic sandstone of the Montonga Formation, the andesite deposits of the Nhlebela Formation, and the tidal deposits of the White Mfolozi Formation (Hicks et al., 2011).

The White Mfolozi Formation is a volcano-sedimentary succession comprised of altering layers of volcaniclastic sandstone, shale, quartz arenite, and stromatolitic dolostone. The quartz arenite in this unit is medium- to fine-grained and well rounded, and contains cross beds, herringbone cross beds, ripple marks, and flaser and lenticular bedding. These features are consistent with formation by deposition and reworking by tidal currents (Balazas and Klein, 1972; von Brunn and Mason, 1977; Hicks and Hofmann., 2011). The stromatolitic carbonate unit is in the upper part of the formation and likely formed in intertidal and shallow subtidal settings (Beukes and Lowe, 1989). Stratifrom, domal, columnar, and conical stromatolites composed of interlaminated grey dolostones and chert are common in this unit (Beukes and Lowe, 1989). The dolostone and chert are secondary lithologies formed after the growth of the stromatolite, with dolostone formed by the replacement of calcium carbonate by dolomite, and chert formed by replacement of some carbonate and other primary materials were replaced by chert during silicification (Beukes and Lowe, 1989). Stromatolitic laminations

commonly contain admixed siliclastic grains interpreted to have been trapped and bound

by microbial mats (von Brunn and Mason, 1977; Beukes and Lowe, 1989).

3. METHODS

In order to analyze elemental distributions in Nsuze Group stromatolites, a large block was collected along the White Mfolozi River, South Africa, and cut into three slabs approximately 1 cm thick. Each slab face was scanned by µXRF (Horiba XGT-7000). Scans were performed at a resolution of 100 µm over 5.12×5.12 cm² to duplicate the resolution of PIXL. 10-µm-resolution scans over 5.12×5.12 mm² were done to investigate fine-scale details. The X-ray generator uses a rhodium block as a target material for generating X-rays, an accelerating tube voltage of 50 kV and a filament current of 1 mA. Full spectra from 0-40 keV were collected at each point with a duration time of .02-0.05 s over 8-16 accumulations. Resulting fluorescence maps were analyzed using ImageJ Software (Rasband, 2014).

The µXRF used for this study and PIXL are similar in that both use Rh as the target material and produce fluorescence elemental scans at approximately 100 µm resolution. However, PIXL will use a tube voltage of 28 kV and a filament current of 200 µA. The higher voltage and current used in this study produce a more intense fluorescence and thus allows for data collection over a shorter period of time. PIXL also scans smaller areas by directing an X-ray beam from a stationary position across a stationary target, causing the angle of incidence to change across the scanning surface and changing the measurement resolution slightly away from the center of the target. In contrast, the Horiba µXRF rasters the target below a stationary X-ray beam, producing constant spatial resolution for flat samples such as the ones in this study.

9

Fluorescence microfacies were defined by elemental associations with each other and with physical structures. Individual fluorescence microfacies were examined to identify correlations between different elements, textures and/or morphologies and processes resulting from the development of the stromatolite.

Thin sections were made to aid in the analysis of the stromatolites samples. Petrographic analysis was performed to confirm or refine mineral grain identifications from μXRF scans.

4. RESULTS

4.1 Fluorescence Microfacies

Ca, Si, K, Fe, S, Mn, Mg, Ti, and Zr were all detected in the Nsuze Group samples (Fig. 4.1) and used to sub-divide it into five fluorescence microfacies: laminated dolostone, laminated chert, clotted dolostone and chert, stromatolite clast breccia, and cavity fill (Fig. 4.2; 4.3; 4.4).
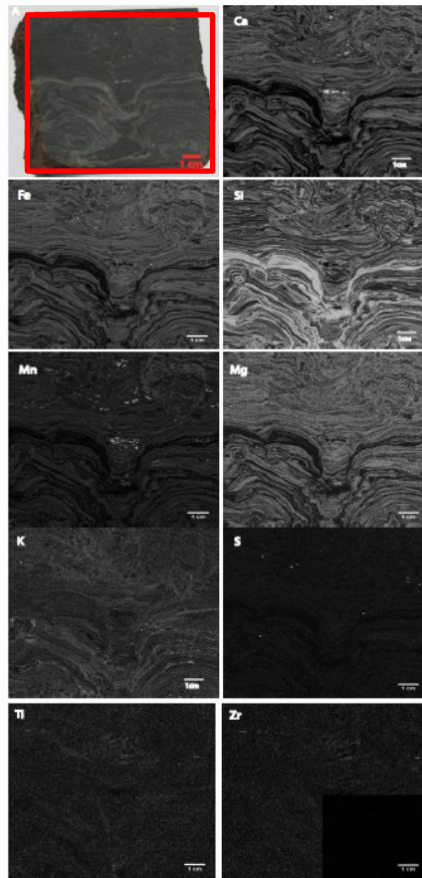
Figure 4.1. Photograph of a slab cut through Nsuze Group stromatolite sample. (The boxed area is the location of XRF scan) (A) with 100 μm resolution elemental fluorescence maps of the same face. Ca, Si, K, Fe, S, Mn, Mg, Ti, and Zr were all detected in the Nsuze sample.
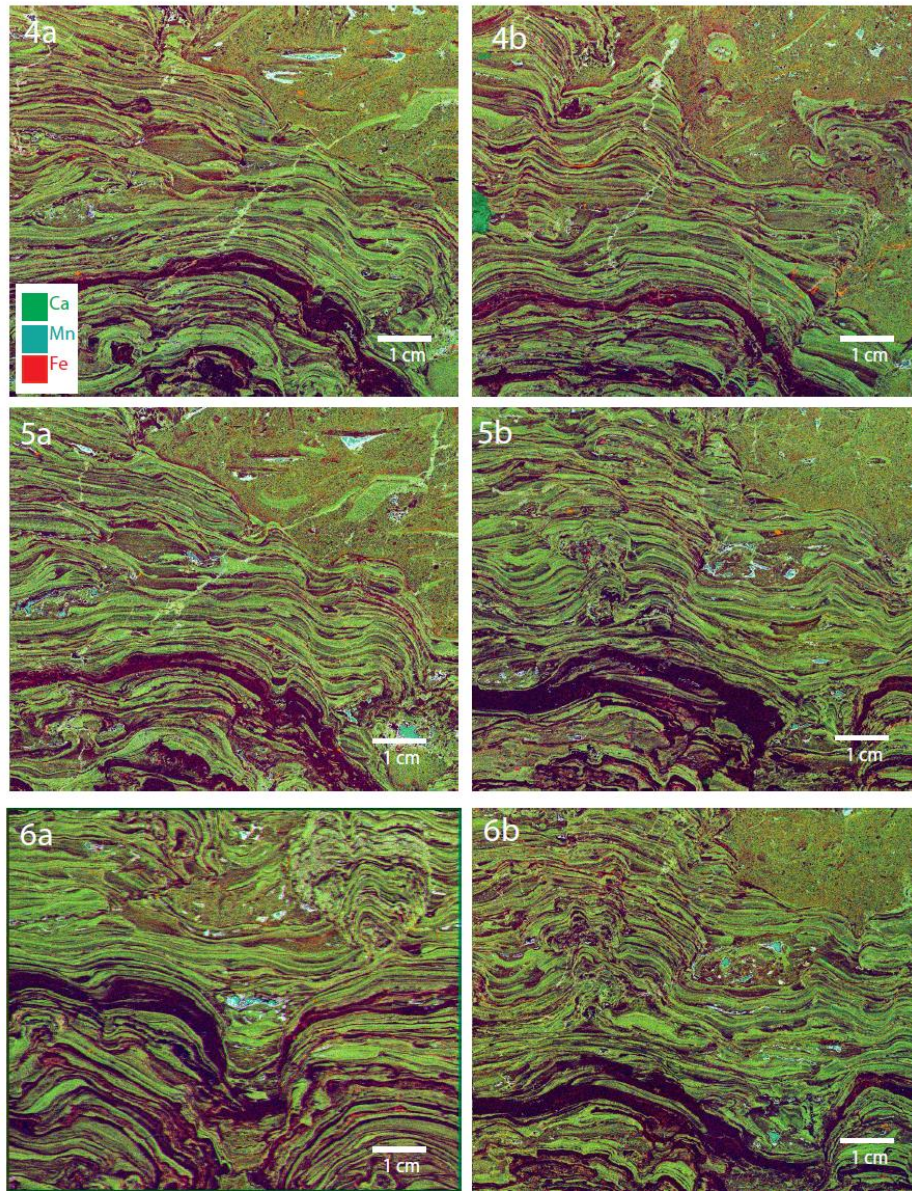
Figure 4.2. False color images of slabs from the Nsuze sample. Green layers are dolostone, black layers are chert and light blue is Mn-rich cavity fill.
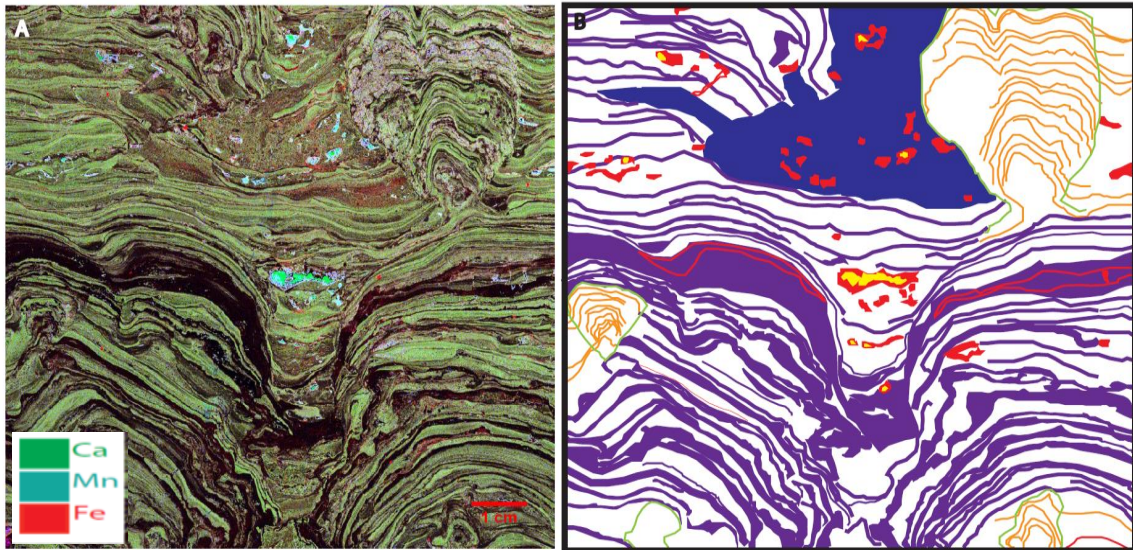
Figure 4.3. Fluorescence facies distributions. (A) False color image of the 6a slab face. (B) Fluorescence microfacies map for the 6a slab. The sample was divided into six fluorescence microfacies: laminated dolostone (white), laminated chert (purple), clotted dolostone and chert (outlined in orange), stromatolite clast breccia (blue), and cavity fill (red highlights Mn-rich dolomite and microquartz; yellow highlights calcite).
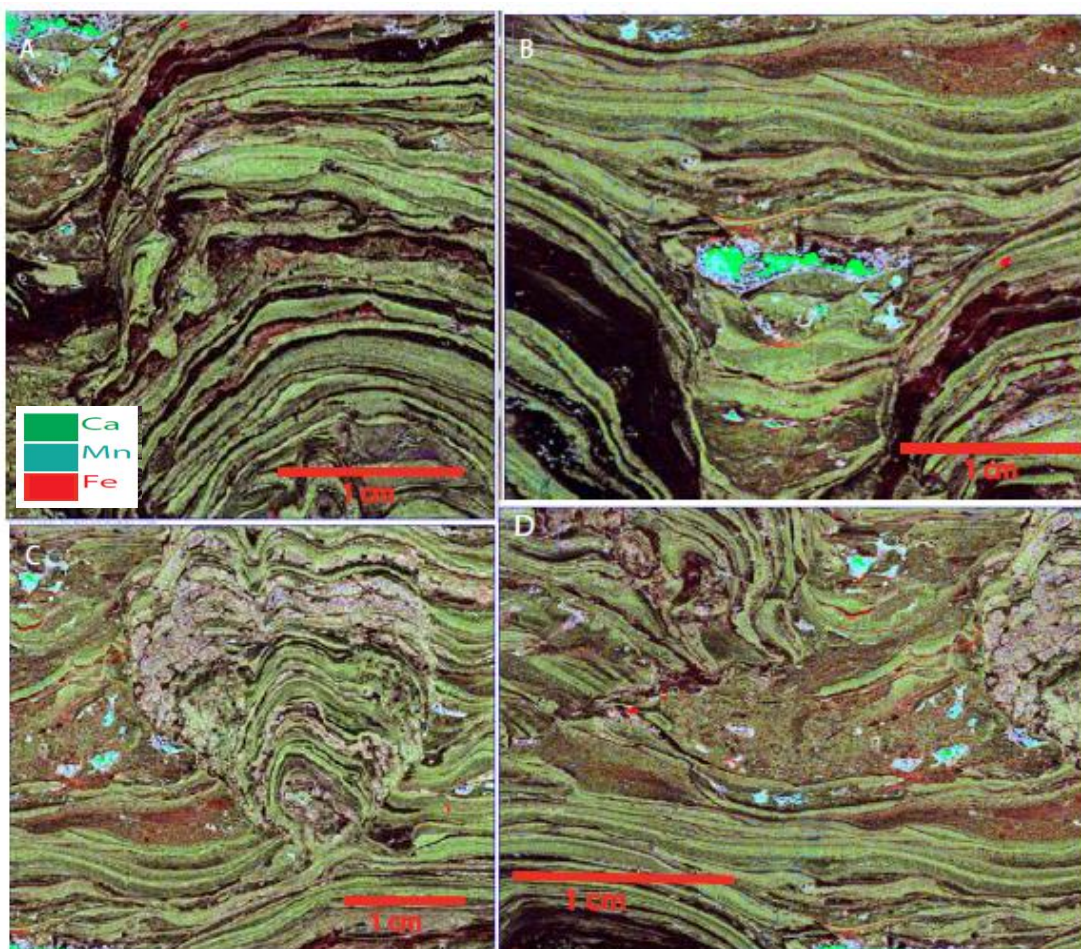
Figure 4.4. False color images of the 6a slab face. The stromatolite was subdivided into: laminated dolostone (A), laminated chert (A), Mn-rich dolomitic cavity fill (B), calcitic cavity fill (B) clotted dolostone and chert (C), stromatolite clast breccia (D). Green layers are dolostone, black layers are chert and light blue is Mn-rich cavity fill. The red Fe-rich are pyrite and carbonate grains are present in the chert laminations.

4.1.1 Laminated Dolostone

Descriptions: Common elements in the laminated dolostone fluorescence facies are Ca, Fe, Si, K, Ti, and Zr. Ca, Mg, Fe, and Mn distributions are highly correlated in this facies, implying that the Fe and Mn are a part of the dolomite (Fig. 4.4A). Coarse

14

(500-700 μm), randomly dispersed Fe- and S-rich grains (pyrite) occur (Fig. 4.1Fe, S). Some Fe also occurs in unidentified isolated grains. Si-rich grains occur in the dolostone laminations, most likely in quartz, and commonly define microlaminations within larger dolomitic laminations (Fig. 4.5A). The occurrence of contrasting sediment types allows for visualization of sedimentary structures in the dolomitic laminations that would otherwise be impossible to detect, such as grading, laminations, and cross laminations (Fig. 4.5A). Syndepositional slumps (Fig. 4.5C) and faults (Fig. 4.5C) occur on the tops of both small domes, whereas dolostone chip breccia occurs on dome flanks (Fig. 4.5D). Ti and Zr are dispersed in isolated grains having sizes similar to the resolution of the μXRF probe head (100 μm) throughout the laminations and are likely present as rutile or anatase and zircon grains, respectively (Fig. 4.6). Very fine K-rich minerals line lamination boundaries and are inferred to represent drapes of K-rich phyllosilicate minerals (Fig. 4.1K). Individual dolomitic laminations frequently form slopes greater than the angle of repose for unconsolidated sediment (Fig. 4.3A).
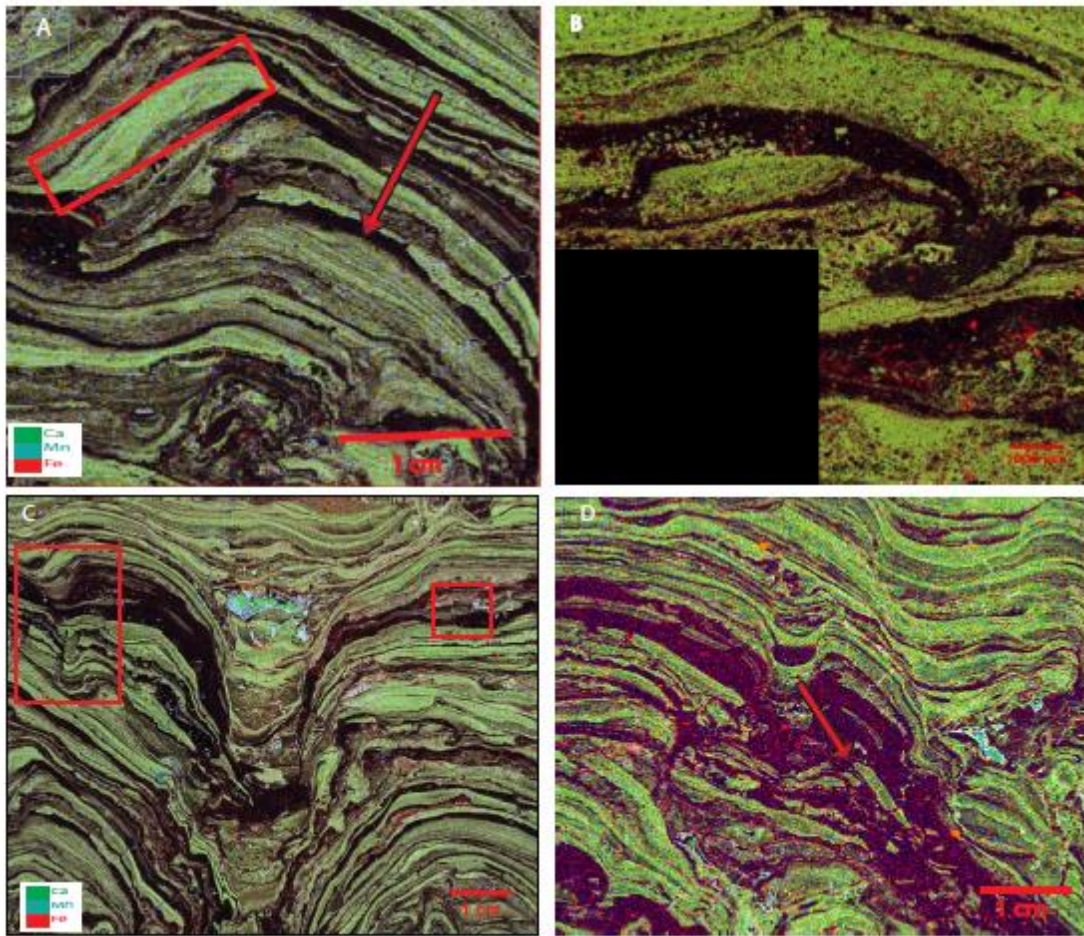
Figure 4.5. Fe (red), Ca (green), and Mn (blue) false color images of sedimentary structures in the laminated dolostone facies. Common sedimentary structures are cross laminations and compositional grading (A), 10 μm resolution image of a rolled chert in laminated dolostone interpreted as a microbial roll-up structure (B), syndepositional faults (left) and slumps (right) structure are boxed (C), and dolostone chip breccia (D).
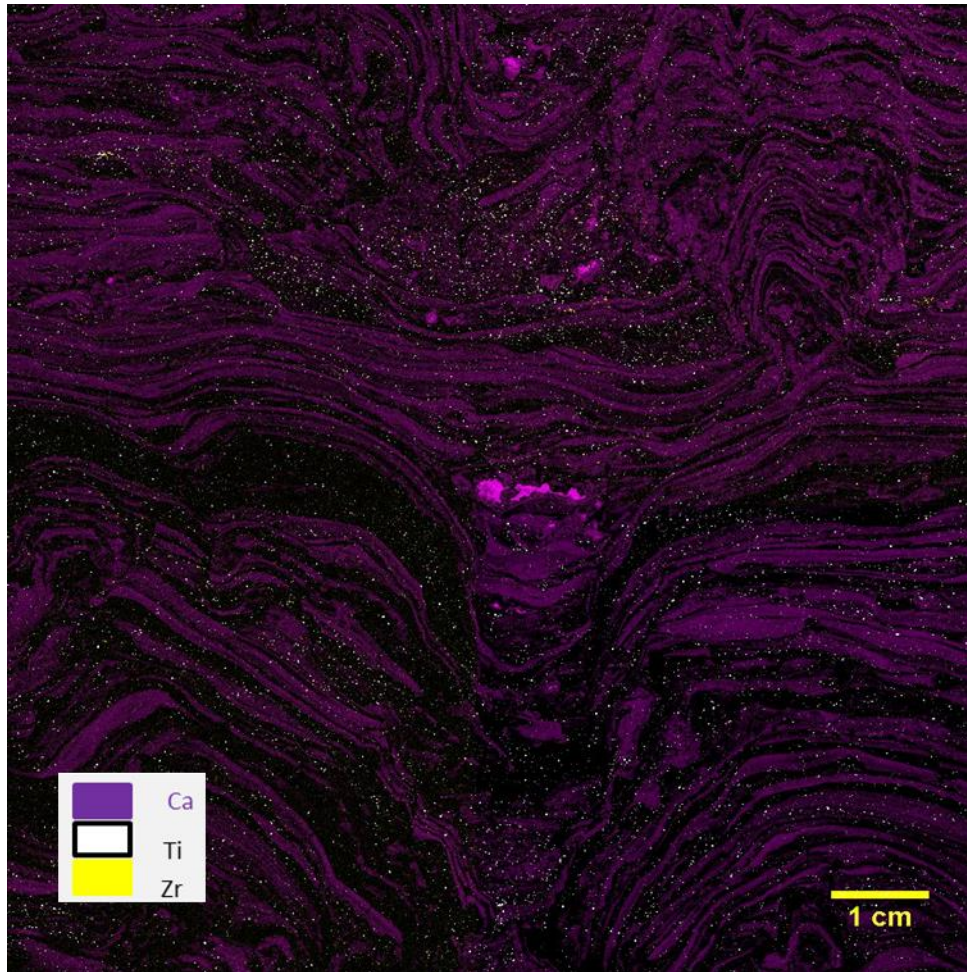
Figure 4.6. False color image showing distributions of Ti and Zr with respect to dolostone (magenta) and chert (black) layers. Field of view as in Fig. 4.3. Ti and Zr are disseminated throughout the laminations, and mark the presence of heavy minerals.

Interpretation: This fluorescence microfacies was likely formed primarily by the growth of microbial mats that trapped and bound siliciclastic sediment and precipitated of micritic carbonate cement. Mats produced cohesive layers and highly inclined surfaces. A single layer containing truncated cross laminated dolomite (Fig. 4.5A) indicates rare instances of bed-load transport and deposition of sand-sized carbonate grains.

Syndepositional slumps, faults, and dolostone chip breccias are contained in one layer of the stromatolite marking disturbance by a single event that induced both plastic and brittle deformation. The variation in deformation style suggests a steep gradient in material properties near the sediment/water interface, with a shallow cohesive layer capable of flow and a lithified layer <2 cm below the surface. The strength gradient with respect to distance from the stromatolite surface was steeper on the flanks, producing more brittle failure along dome margins than on dome tops, where slumping dominated (Dillion and Zimmerman, 1970).

Pyrite grains were unlikely to have been transported by currents based on comparison to co-occurring grain types. Carbonate grains had a maximum diameter of 300 μm based on the maximum thickness of laminations in the cross laminated dolostone layer. The ratio of the Stokes settling velocities of the pyrite grains (ρ_{pyr}= 5.0 g cm^{-3}) to carbonate grains (ρ_{carb}= 2.7-2.9 g cm^{-3}), using the maximum inferred diameters, is ~8.9 (Eq. 4.1).

$$\frac{\omega_{\text{pyr}}}{\omega_{\text{carb}}} = \frac{(\rho_{\text{pyr}} - \rho_{\text{water}})d_{\text{pyr}}^2}{(\rho_{\text{carb}} - \rho_{\text{water}})d_{\text{carb}}^2}$$

Equation 4.1

Here, ρ_{pyr}, ρ_{carb}, and ρ_{water} are the densities of pyrite, carbonate, and water, respectively; d_{pyr} and d_{carb} are the diameters of pyrite and carbonate grains; and ω_{pyr} and ω_{carb} are the Stokes settling velocities of pyrite and carbonate grains.

The Rouse number (Eq. 4.2) of a grain relates the hydraulic properties of a flow and grain properties to transport mechanisms. Here, ω_s is the setting velocity of the grain; k is the von Kármán constant; u_* is the shear velocity of the fluid, and R_{pyr} and R_{carb} are the Rouse numbers for pyrite and carbonate grains. R_o greater than 6.25 indicate bed load transport; R_o between 6.25 and 1 indicates mixed load transport; and R_o less than 1 indicates suspended load transport. By comparing the ratios of the Stoke's setting velocity and the Rouse number of the pyrite grains to the carbonate grains and allowing R_{pyr} to equal the minimum value for bed load transport, the Rouse number of the carbonate grains is 0.7 (Eq. 4.3). The carbonate grain would therefore be transported by suspended load if the pyrite grains were transported by bed load. Therefore, these grains are not hydraulically equivalent and would not have been deposited by the same current (Allen, 1968; Julien, 1995).

$$\frac{\omega_s}{ku_*} = R_o \qquad\qquad \text{Equation 4.2}$$

$$\frac{R_{opyr}}{R_{ocarb}} = \frac{\omega_{pyr}}{\omega_{carb}} \qquad\qquad \text{Equation 4.3}$$

Alternatively, if the pyrite had recrystallized from primary grains 100 μm in diameter, they would have had similar settling velocities and facies distributions to zircon (ρ_{zircon}= 4.7 g cm^{-3}) and rutile (ρ_{rutile}= 4.2 g cm^{-3}) grains. Instead, pyrite is distributed randomly and sparsely in the laminated dolostone fluorescence microfacies, whereas zircon and rutile are distributed along microlaminations, in interstromatolite spaces, and in stromatolite clast breccias (Fig. 4.6). Pyrite is therefore interpreted to have formed by *in situ* precipitation and does not reflect the oxidation state of the overlying water column during stromatolite growth.

4.1.2 Laminated Chert

Description: The primary element detected in the laminated chert fluorescence microfacies is Si, although other elements associated with siliclastic grains (K, Ti, Zr) occur in laminations and lenses of fine-grained phyllosilicates (Fig. 4.1K), randomly disseminated heavy minerals (Fig. 4.6), and rare sand-sized K-rich grains (Fig. 4.1K; 4.7). Isolated carbonate grains and unidentified Fe-rich grains also occur in the chert laminations (Fig. 4.5B). Like some dolostone laminations, some chert laminations formed slopes above the angle of repose for unconsolidated sediment (Fig. 4.3A). Some chert laminations include 2-4 mm tall peaked structures that are vertically oriented on both the tops and sloping flanks of domes (Fig. 4.4A). Dolostone laminations sometimes terminate or lap onto these peaks (Fig. 4.5A). Some peaks contain sand-size K-rich grains organized into small conical piles 2-3 grains deep (Fig. 4.7). Partially rolled up chert chips occur in a single dolostone lamination (Fig. 4.5B).
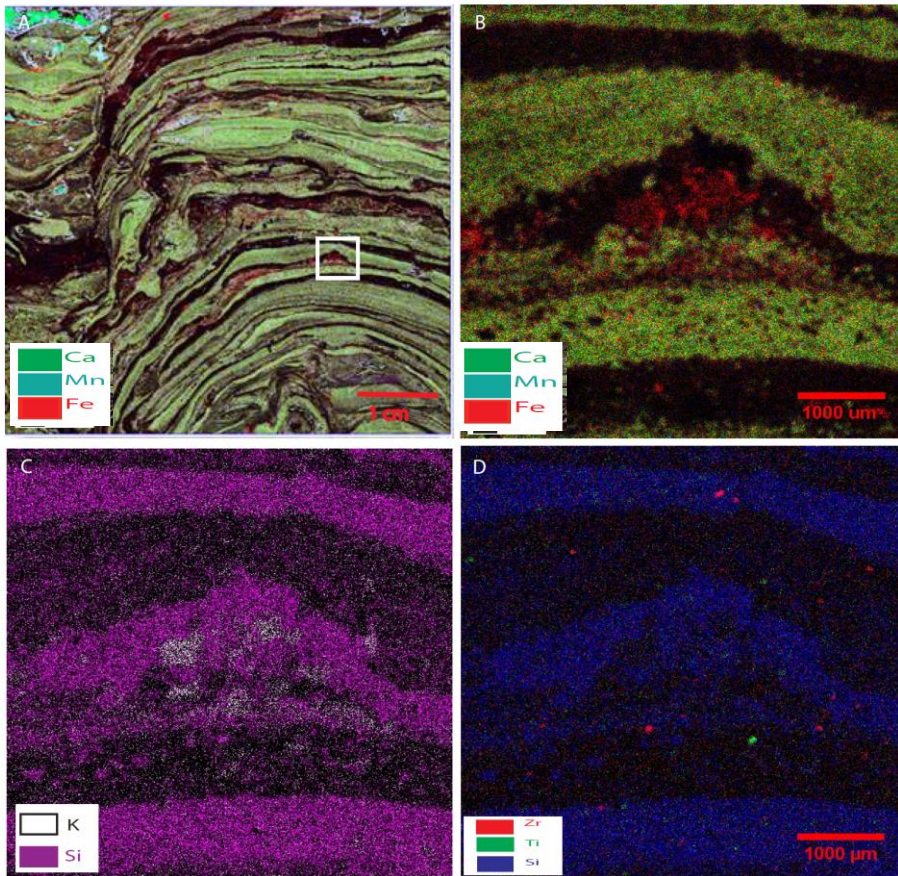
Figure 4.7. Peaked structures in the laminated chert fluorescence microfacies. (A) False color image of the lower right side of 6a slab face highlighting 2-mm-tall peak (box). Color as in Fig. 4.2. B-D. 10 μm resolution false color images of the boxed area in image A. Peak contains a small pile of K- and Fe-rich sand-sized grains. Similar grains were identified petrographiclly as sericite micromosaics representing devitirififed volcaniclastic grains.

Interpretation: The chert in the laminated chert fluorescence microfacies formed during silicification of a preexisting material that was cohesive as indicated by oversteepened layers. It also flowed plastically as indicated by the presence of floating dolostone chips in disrupted chert laminations (Fig. 4.3A; 4.5D). Rare rolled up chert bodies are consistent with this interpretation, and likely represent microbial roll-up

structures (Sumner, 1997; Simonson and Carney; 1999; Tice and Lowe, 2004; Bosak, et al., 2013a). Uniform orientation of chert peaks and their effect on the distribution of detrital sediment cannot be explained by formation by slumping, soft sediment deformation, or diagenesis; instead, they likely formed as microbial cones or pinnacles. These inferences suggest that the laminated chert fluorescence microfacies represents silicified microbial mat that incorporated little to no sand-size detrital material, although it is possible that some trapped or precipitated micrite was present and later replaced during silicification (Knoll, 1985; Heidari et al. 2010).

4.1.3 Clotted Dolostone and Chert

Description: The clotted dolostone and chert fluorescence microfacies is composed of high-relief cauliform mounds composed of intergrown dolomite and chert forming clots and cryptically laminated clots (Fig. 4.8). Cryptic laminations can be vertical or even overhanging. This fluorescence microfacies contains abundant cavities filled with Mn-rich dolomite of the cavity fill fluorescence microfacies (Fig. 4.4C). Minor K is present, likely in fine-grained phyllosilicates (Fig. 4.8). Clotted dolostone and chert fluorescence microfacies form the core of each stromatolite and each branch off of an underlying domal stromatolite. From threshold maps of Mn and Si, the porosity of the clotted microfacies was estimated to range from 37-50%.
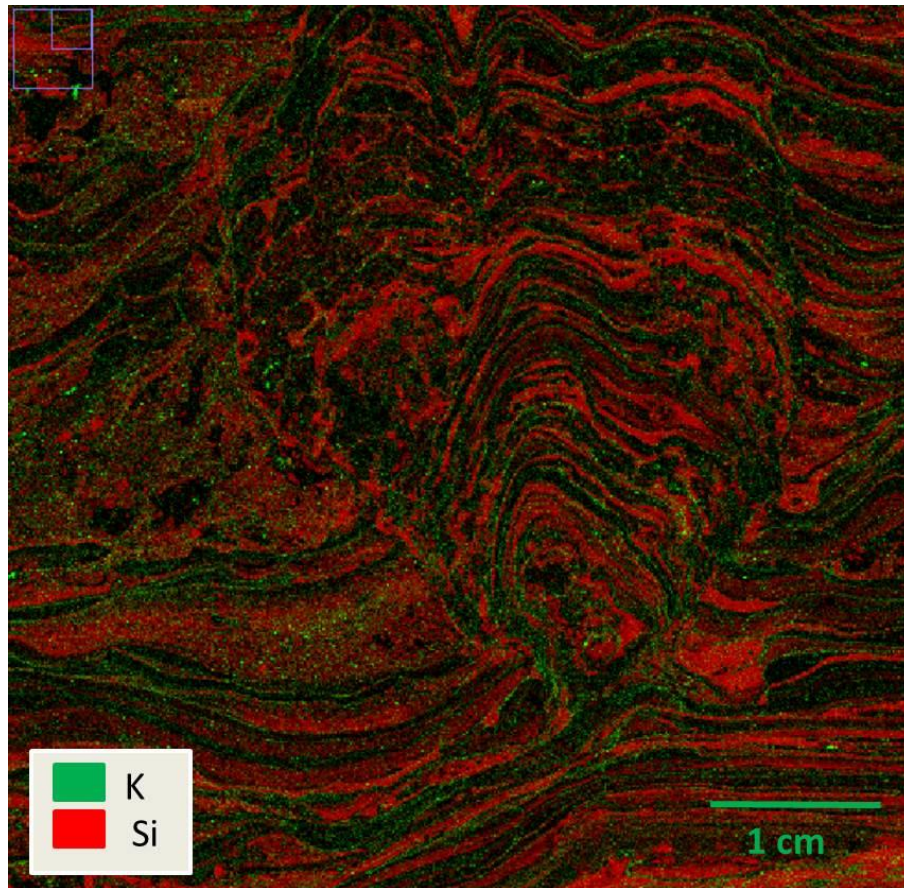
Figure 4.8. False color image showing distribution of fine K-rich material in a large high-relief cauliform mound composed of clotted dolostone and chert (upper right corner on the 6a slab face). The clotted parts of this structure are produced mainly by precipitation. Clotted areas are cryptically laminated.

Interpretation: The cryptic laminations in this fluorescence microfacies were likely the primary structure formed by precipitation and mat growth. The clotted structures were likely secondary and formed by *in situ* precipitation of carbonate minerals and by silicification. Enhanced porosity in the clots could have been created by decomposition of the mat or partial collapse or dissolution of the mat cement.

4.1.4 Stromatolite Clast Breccia

Description: The stromatolite clast breccia fluorescence facies is a breccia composed of stromatolite clasts supported by a massive matrix composed of mixed chert and dolomite and containing an abundance of heavy mineral grains and unidentified Fe-rich grains (Fig. 4.4; 4.6). This facies fills erosional scours and space between stromatolites. The stromatolite clast breccia hosts the majority of the large cavities filled by the cavity fill fluorescence microfacies (Fig. 4.4D).

Interpretation: This facies was deposited when energetic currents eroded stromatolites and other sediment and rapidly redeposited them as lags in topographic lows with little to no sorting. The large cavities could have formed by the dissolution of carbonate during silicification or from decomposition of eroded mat chunks.

4.1.5 Cavity Fill

Description: Cavities in both the clotted dolostone and chert and stromatolite clast breccia fluorescence microfacies are filled with intergrown Mn-rich dolomite and microquartz, and where cavities are larger than ~0.5 mm, by an inner core of partially dolomitized calcite (Fig. 4.4B).

Interpretation: The Mn- rich cavity fill fluorescence microfacies likely reflects the composition of near surface pore water that filled pore spaces during early diagenesis. Calcite cavity fill reflects changing pore water compositions during early burial.

4.2 Fluorescence Microfacies Thin Section Analysis

Laminated dolomite is comprised of alternating laminations of ~30-200 μm sized dolomite grains, including euhedral to subhedral rhombs in several locations (Fig. 4.10A), and microquartz laminations (Fig. 4.10C). Very fine quartz grains (~50-100 μm) are occur in some laminations (Fig. 4.10C). Fine K-rich grains were identified as sericite clay (Fig. 4.10B), which is common in the Nsuze Group. Sericite drapes mark some of the boundaries between dolostone and chert laminations (Fig. 4.11C; D).

The primary Si-bearing phase in the laminated chert is microquartz (Fig. 4.9), although the microfacies also locally contains very fine to fine quartz grains (~70-140 μm) and dolomite crystals (~70-130 μm) (Fig. 4.9A; 4.11A). Phyllosilicate minerals draped the boundary between dolostone and chert laminations and were identified as sericite. Medium to coarse size K-rich grains (~200-550 μm) were identified as masses of intergrown fine sericite (Fig. 4.10B). The grains were likely formed by the alteration of vitric volcaniclastic grains.

The clotted dolostone and chert microfacies as seen in thin section had similar geometries to those observed by μXRF. Clots were comprised of clusters of dolomite rhombs with intergrown quartz. Dolomite appeared similar to dolomite from other microfacies (Fig. 4.12).
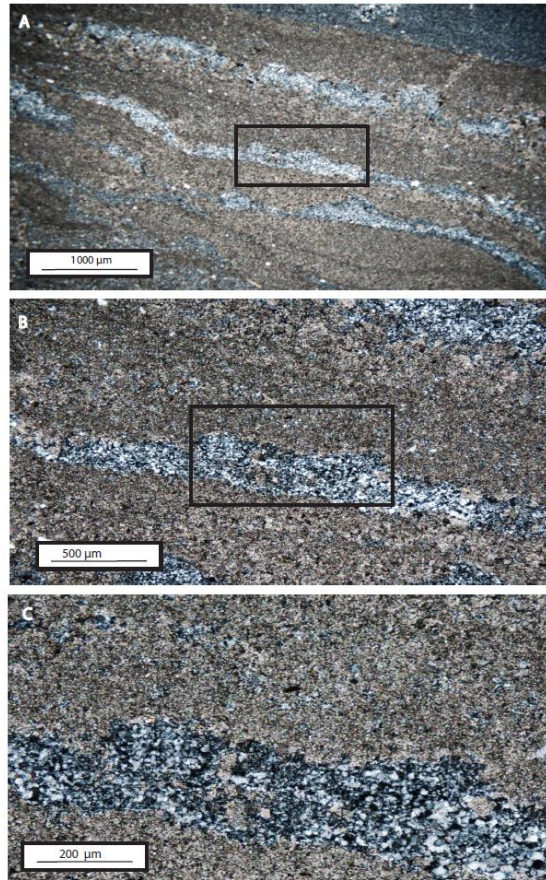
Figure 4.9. Petrographic images of interlaminated dolostone and chert in cross-polarized light. (A) Dolostone (brown) and chert (grey) laminations. The rectangle highlights the area magnified in image B. (B) Detailed images showing the contact between the dolostone and chert laminations. Quartz grains are present in the dolostone laminations. The rectangle highlights the area magnified in image C. (C) Dolomite grains suspended in chert. Dolostone laminations are composed of dolomicrite. Both the dolomite and chert are secondary lithologies.
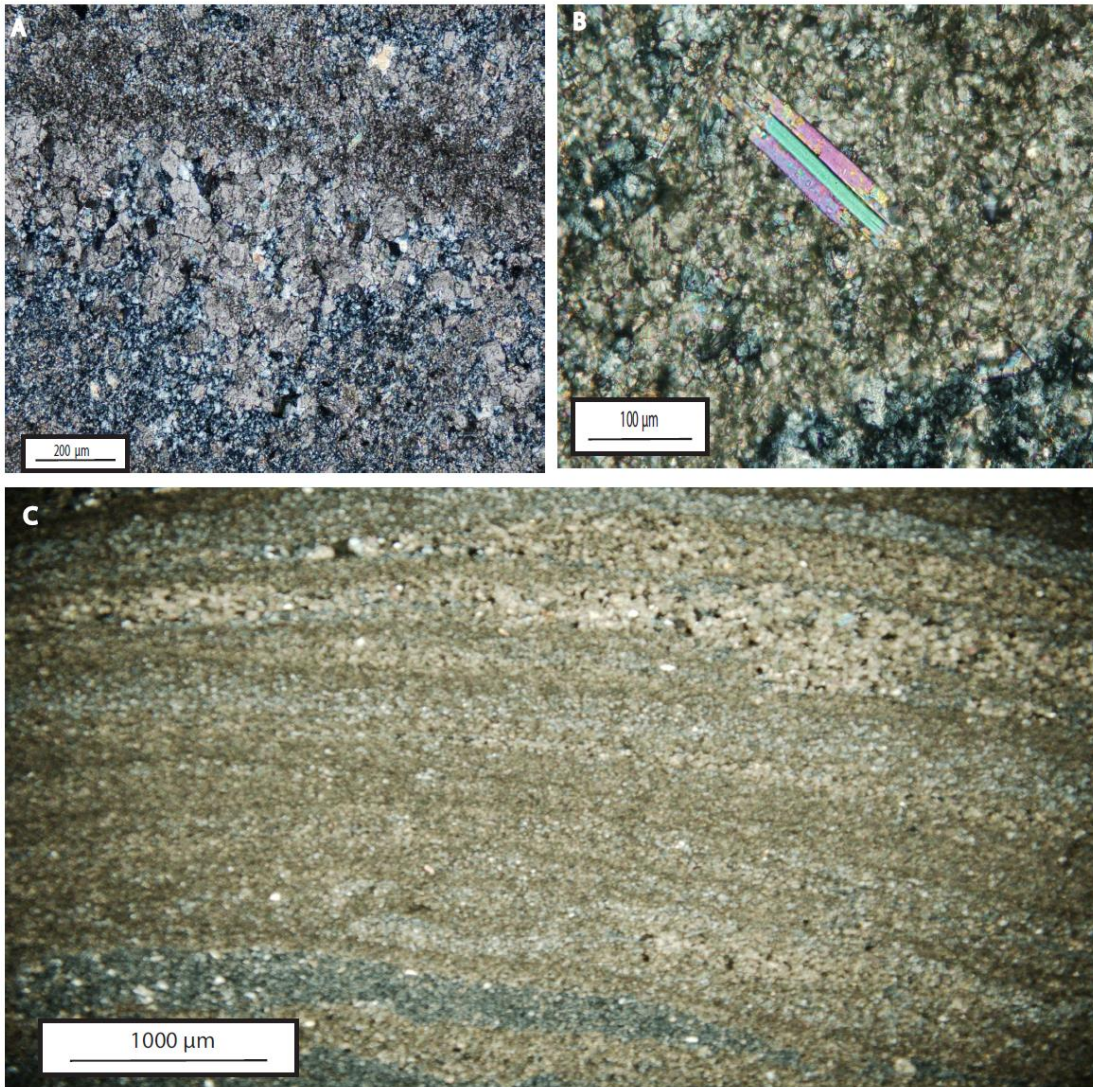
Figure 4.10. (A) Petrographic (cross-polarized) image of dolomites rhombs at the contact between dolostone and chert laminations. (B) Sericite grain in a dolostone lamination, associated with clay minerals. (C) Microlaminations of quartz grains within larger dolomitic laminations; these contrasting sediment types allow for visualization of sedimentary structures present in the dolomitic lamination.
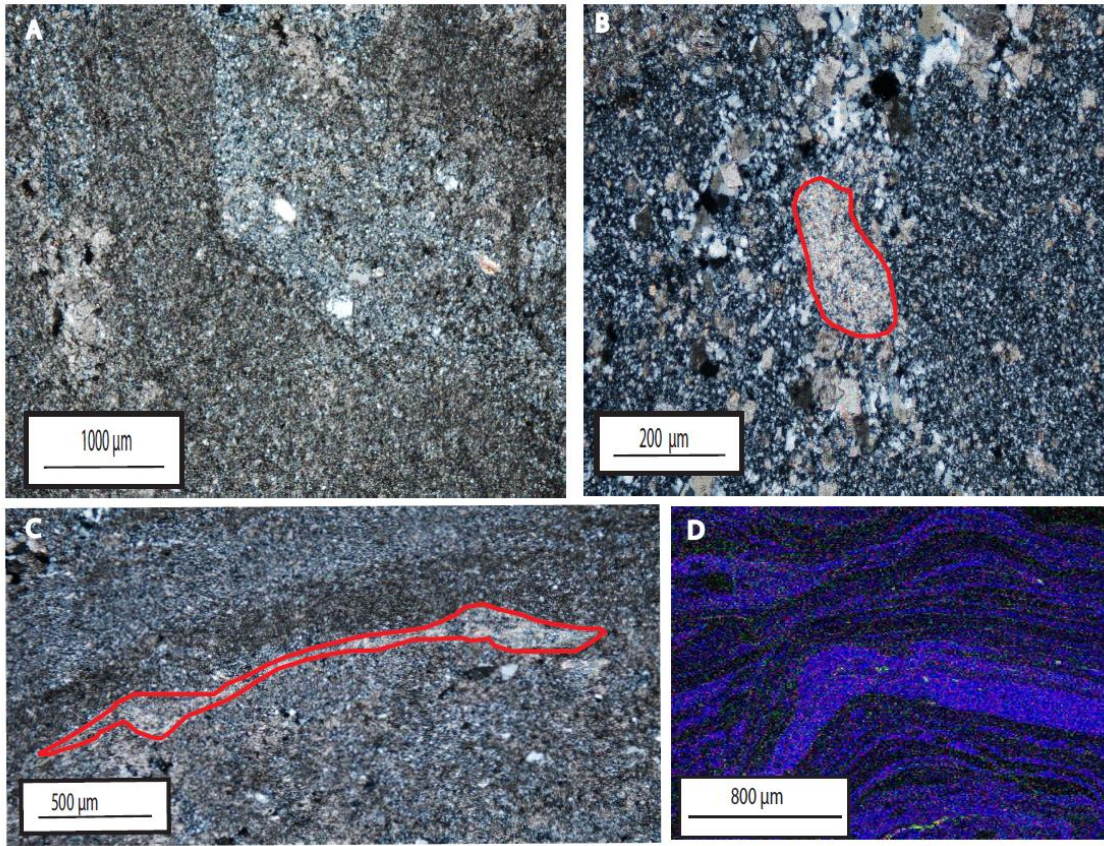
Figure 4.11. (A) Quartz grains in chert lamination. The distinction between chert and quartz was only observed in the thin sections and cannot be seen on Si elemental µXRF scans. (B) Sericite clast floating in chert lamination. The K-rich grains, from the XRF scans (D) were identified as medium to coarse size sericite clasts. (C) Petrographic images of the K-rich sericite drape (D) at the boundary of a chert and dolostone lamination. (D) 100 m false color image of K (green) and Si (blue), from a thin section (top of KQ_NSZ_2).
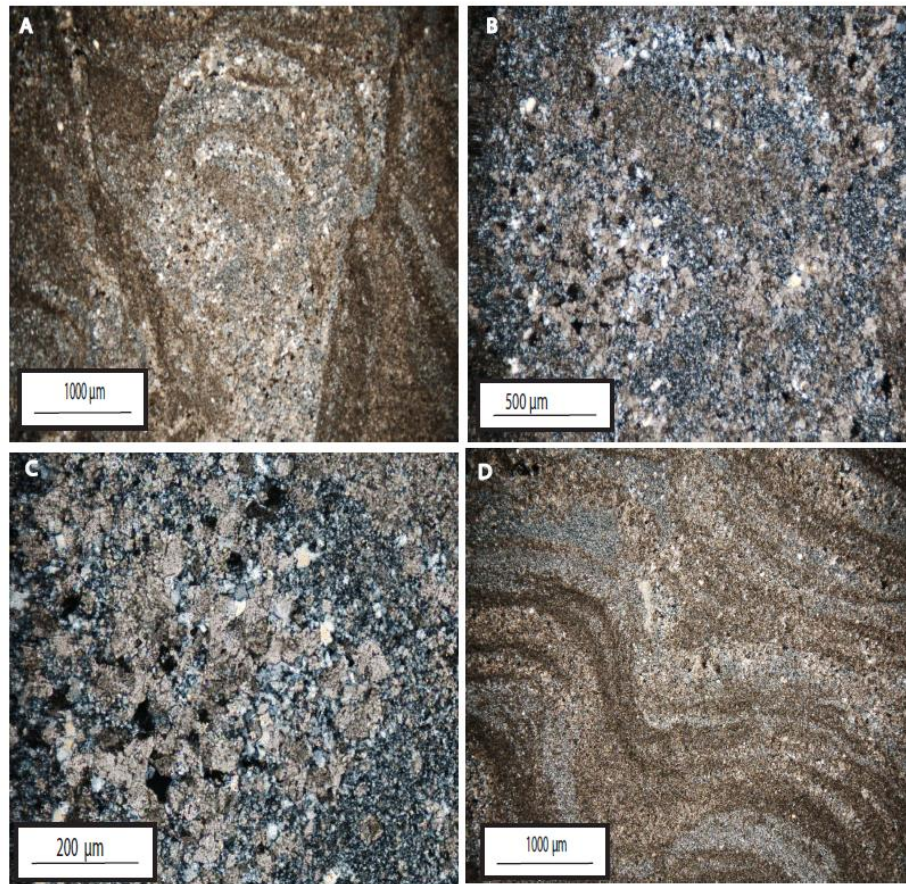
Figure 4.12. Petrographic, cross-polarized images of the clotted dolostone and chert facies (from thin section KQ_NSZ_1). (A) Image showing the interaction between the clotted dolostone and chert fluorescence microfacies and the surrounding dolostone and chert laminated fluorescence microfacies. (B) Detailed images of clotted structure in the mound. (C) Detailed image of dolomite in clotted structure. Secondary dolomite is intimately intergrown with microquartz. (D) Image of interlaminated dolostone and chert covering the clotted mound.

5. DISCUSSION

5.1 Nsuze Group Growth Model

Domal stromatolites in the Nsuze Group samples were built by the cyclic accumulation of precipitated and mat-stabilized micrite, now preserved as laminated dolomite layers, and clastic-poor microbial mats, now preserved as secondary laminated chert layers. Alternating clastic-rich dolostone layer and clastic–poor mat layers likely reflect changing current intensities and sediment supply relative to mat growth rate.

The combination of plastic failure at shallow depths in the stromatolites and brittle failure at slightly greater depths was likely related to different sources of material strength in each zone. In the shallow zone, strength likely resulted from the cohesion of the microbial mat itself, i.e. from the presence of extracellular polymeric substances produced by microorganisms and potentially form intergrown filamentous organisms (Tice et al., 2011). In the deep zone, strength likely resulted from precipitation of early diagenetic carbonate cements that lithified the mat. In modern mats, cementation at depth often occurs as mats decompose, often during sulfate reduction (Riding, 2000; Dupraz et al., 2009; Dupraz et al., 2013). In the low-sulfate oceans of the Mesoarchean (Habicht et al., 2000; Kah et al., 2004), cementation may have been associated with iron reduction (Olsen, 2006; Zeng and Tice, 2014). In either case, the transition from plastic to brittle deformation in Nsuze Group stromatolites likely occurred at, or near, the boundary between net autotrophic production of organic matter in the shallow mat and net heterotrophic oxidation of organic matter in the deep mat, and thus reflected metabolic zonation within the original mat communities. The strength gradient inferred

for one dolostone layer suggests that the transition between the autotrophic and

heterotrophic layers of the mat varied in thickness systematically from the tops to the

flanks of domes. On the top of the dome, the net autotrophic layer was thicker, resulting

in a thicker plastic zone and a deeper brittle zone. On the flanks the autotrophic zone was

thinner, resulting in more brittle deformation for the same depth of disturbance. This

overall trend in thickness in metabolic zones within the mats paralleled trends in

dolostone and chert layer thicknesses from domes to flanks, suggesting that dolostone

and chert layer thicknesses were ultimately controlled by spatial gradients in net mat

accumulation rate (Fig. 5.1A; B.).
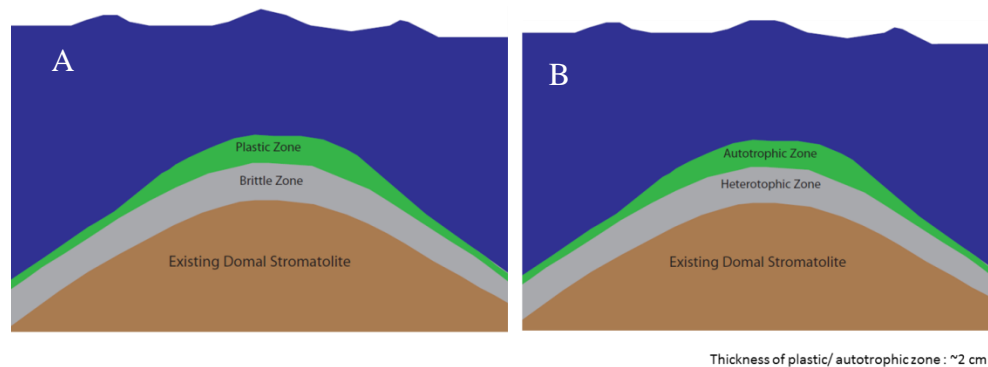
Figure 5.1. (A) Plastic failure (green) at shallow depths in the stromatolites and brittle failure (grey) at slightly greater depths was likely related to different sources of material strength in each zone. In the shallow zone, strength likely resulted from the cohesion of the microbial mat itself. In the deep zone, strength likely resulted from precipitation of early diagenetic carbonate cements that lithified the mat. (B) The transition from plastic to brittle deformation in Nsuze Group stromatolites likely occurred at or near the boundary between net autotrophic production of organic matter in the shallow mat and net heterotrophic oxidation of organic matter in the deep mat, and thus reflected metabolic zonation within the original mat communities. The strength gradient inferred for one dolostone layer suggests that the varies in thickness systematically from the tops to the flanks of domes.

Domal stromatolite growth maintained constant synoptic relief above surrounding sediment as long as mat growth, precipitation, and sediment trapping and binding kept pace with accumulation of detrital material between domes. Constant synoptic relief is shown by the continued upward growth of dolostone and chert laminations and the maintained domal structure of the stromatolite, as detrital grains are deposited in the space between the dome. In the sample examined, domes began to drown when dolostone layers began to thicken between domes and thin onto their tops. Laminated chert layers are less common in sediments deposited during this time, suggesting that the supply of carbonate sediment had increased, likely due to increased ambient current activity. Relatively flat dolostone layers dominate at this point, consistent with predictions of mat flattening under high-shear currents (Tice et al., 2011).

New stromatolites were seeded by the growth of high-relief cauliform clotted structures which formed shrub-like projections on the sea floor and templated subsequent accumulation of laminated stromatolites. It is not clear what produced the characteristic clotted fabric of these early structures, but their cryptic lamination and high early porosity suggest that it may have a diagenetic origin. They are here interpreted as thrombolites, making them the oldest known thrombolites by ~1 Ga (Kah and Grotzinger, 1992).

Traditional petrographic analysis supported many of the observations and interpretations made based solely by μXRF analysis; however, some observations were possible only with one technique. Because they did not contrast in composition, quartz

sand grains in chert laminations were not detected by µXRF, rather siliciclastic content had to be inferred from Ti-, Zr-, and K-rich grains. Sand-sized K-rich grains were not identifiable from µXRF alone; they were identified as sericitized volcaniclastic grains only optically. The K-rich grains in the thin section were in a different lamination than the grains in the XRF. However, large feldspar grains do not occur in thin sections, suggesting that the grains in the µXRF were sericite.

µXRF analysis revealed possible metabolic zonation with a cemented heterotrophic layer and varying thickness of the autotrophic layer. This interpretation was made by analysis of the chert and dolostone laminations from µXRF scans. XRF also identify distinct generations of dolomite based on differential Mn content, even though they were optically identical. The ability to make process interpretation will be useful to PIXL during its search for biosignatures on Mars. This research demonstrates that although there are limitations, µXRF spatial relationships of the elements and elemental composition can be used to infer specific microbial growth processes

6. CONCLUSIONS

PIXL 2020 mission is approaching; so understanding the strengths and weaknesses of the mesoscale XRF chemical scans is valuable. This technique helped highlight sedimentary features and the spatial relationships of the elements that can't be seen in outcrop, hand sample or thin section. Highlighting those structures and relationship lead to development of a more complete process interpretation for the formation of the Nsuze Group stromatolite.

The µXRF scans and previous description of stromatolites from the Nsuze Group indicated variations in the stromatolite lithologies (i.e. dolostone and chert laminations). These variations allowed for microbial laminations and sedimentary structures to be observed. For example, if the stromatolite was made of dolostone laminations, it would be difficult to observe distinct microbial laminations because of their similar composition. When determining locations on Mars for PIXL to scan, remembering that the µXRF scans can reveal the greatest amount of information when a sample with varying lithologies is scanned is important.

PIXL's mission is to identify microbial biosignatures on Mars using µXRF scans. Microbial biosignatures are measurable trace evidence for microbial presence and processes. The different types of trace evidence were divided into three categories by Cady, 2003. The first category of evidence is whole or partially fossilized of microbial cells. The second is chemical biomarker compounds, organic molecules, and isotope data. The finally category is biofabrics or sedimentary structures resulting from microbial mat processes. In this study, because of the instrument used and the

replacement of most to all of the original minerals in the stromatolite, whole or partially

fossilized of microbial cells and chemical biomarker compounds, organic molecules, and

isotope data were not observed. However, sedimentary structures resulting from

microbial mat processes were imaged through µXRF scans that allowed for the

observation and interpretation of microbial structures and morphologies. This technique

of mesoscale µXRF mapping may therefore be used in the search for life on Mars.

REFERENCES

Allen, J. (1968) The Nature and Origin of Bed Form-Hierarchies. *Sedimentology* 10: 161-182.

Allwood, A.C., Grotzinger, J., Knoll, A.H., Burch, I.W., and Anderson, M.S. (2009) Controls on Development and Diversity of Early Archean Stromatolites. *Proc. Natl. Acad. Sci* 106: 9548–9555.

Balazas, R., and Klein, G. (1972) Roundness-Mineralogical Relations of Some Intidal Sands. *Journal of Sedimentary Petrology* 42: 425-433.

Beukes, N., and Lowe, D. (1989) Environmental Control on Diverse Stromatolite Morphologies in the 3000 Myr Pongola Supergroup, South Africa. *Sedimentology* 36: 383-397.

Bosak, T., Knoll, A.H., and Petroff, A.P. (2013) The Meaning of Stromatolites. *Annual Review of Earth and Planetary Sciences* 41: 21-44.

Bosak, T., Mariotti, G., Macdonald, F., Perron, J., and Pruss, S. (2013) Microbial Sedimentology of Stromatolites in Neoproterozoic Cap Carbonate. *The Paleontological Society Papers* 19: 2-25.

Cady, S., Farmer, J., Grotzinger, J., Schopf, J.W., and Steele, A. (2003) Morphological Biosignatures and the Search for Life on Mars. *Astrobiology* 3: 351-368.

Dillion, W., and Zimmerman, H. (1970) Erosion By Biological Activity in Two New England Submarine Canyons. *Journal of Sedimentary Petrology* 40: 542-547.

Dupraz, C., Fowler, A., Tobias, C., and Visscher, P.T. (2013) Processes of Carbonate Precipitation in Modern Microbial Mats. *Geobiology* 11: 572-548.

Dupraz, C., Reid, R.P., Braissant, O., Decho, A.W., Norman, R.S., and Visscher, P.T. (2009) Processes of Carbonate Precipitation in Modern Microbial Mats. *Earth-Science Reviews* 96: 141-162.

Gattuso, J.P., Frankignoulle, M., Bourge, I., Romaine, S., and Buddemeier, R.W. (1998) Effect of Calcium Carbonate Saturation of Seawater on Coral Calcification. *Global and Planetary Change* 18: 37-46.

Gebelein, C.D. (1969) Distribution, Morphology, and Accretion Rate of Recent Subtidal Algal Stromatolites, Bermuda. *Journal of Sedimentary Petrology* 39: 49-69.

Ginsburg, R.N. (1991) Controversies About Stromatolite: Vices and Virtues. In: *Sedimentology, Earth History and Tectonics*, edited by D, W. Muller. J.A. McKenzie and H. Weissert, Academic Press, London, pp. 25-36.

Grotzinger, J.P., and Knoll, A.H. (1999) Stromatolites in Precambrian Carbonates: Evolutionary Milepost of Environmental Dipsticks. *Annual Review of Earth and Planetary Sciences* 27: 313-358.

Habicht, K., Gade, M., Thamdrup, B., Berg, P., and Canfield, D. E. (2002) Calibration of Sulfate Levels in the Archean Ocean. *Science* 298: 2372-2374.

Heidari, A., Mahbouubi, A., and Moussavi-Harami, R. (2010) Silicification of Carbonate Rocks of Chehel-Kaman Formation (Upper Paleocene) in West of Kopet-Dagh Basin, NE Iran. In: *The 1st Applied Geological Congress, Department of Geology Conference Abstracts*, Islamic Azad University, Mashad Branch, Iran.

Hicks, N., Dunlevey, J., and Liu, K. (2011) A New Stromatolite Occurrence in the Nsuze Group, Pongola Supergroup of Northern Kwazulu-Natal, South Africa. *South Africa Journal of Geology* 114.2: 195-200.

Hicks, N., and Hofmann, A. (2011) Stratigraphy and Provenance of the Aruriferous-Uraniferous, Fluvial to Shallow-Marine Sinqeni Formation, Mozaan Group, Nothern Kwazulu-Natal, South Africa. *South Africa Journal of Geology* 115.3: 327-344.

Hofman, H., Grey, K., Hickman, H., and Thorpe, I. (1999) Origin of 3.4 Ga Coniform Stromatolite in Warrawoona Group, Western Australia. *Geological Society of America Bulletin* 111: 1256-1262.

Hofmann, H.J. (1972) Stromatolites: Characteristics and Utility. *Earth-Science Reviews* 9: 339-373.

Julien, P. (1995) Suspended Load. In: *Erosion and Sedimentation*, Cambridge University Press, United Kingdom, pp. 186-187.

Kah, L., and Grotzinger, J.P. (1992) Early Proterozoic (1.9 Ga) Thrombolites of the Rocknest Formation, Northwest Territories, Canada. *Palaios* 7: 305-315.

Kah, L., Lyons, T.W., and Frank, T.D. (2004) Low Marine Sulphate and Protracted Oxygenation of the Proterozoic Bioshere. *Nature* 431: 834-838.

Kalkowsky, E. (1908) Oolith und Stromatolith im Norddeutschen Buntsandstein: Z. Dutsch Geolo. *Geselschaft* 60: 68-125.

Kawaguchi T., and Decho A.W. (2000) Biochemical Characterization of Cyanobacterial Extracellular Polymers (EPS) from Modern Marine Stromatolites (Bahamas). *Prep. Biochem. Biotechnol* 30: 321-330.

Knoll, A. (1985) Exceptional Preservation of Photosynthetic Organism in Silicified Carbonates and Silicified Peat. *Philosophical Transactions of The Royal Society* 311: 111-122.

Lowe, D., and Tice, M. (2007) Tectonic Controls on Atmospheric, Climatic, and Biological Evolution 3.5- 2.4 Ga. *Precambrian Research* 158: 177-197.

Maliva, R., and Siever, R. (1988) Mechanism and Controls of Fossils in Limestones. *The Journal of Geology* 96: 387-398.

Martin-Algarra, A., and Sanchez-Navas, A. (1995) Phosphate Stromatolites from Condensed Cephalopod: Limestones, Upper Jurassic, Southern Spain. *Sedimentology* 42: 893-919.

Olsen, J.M. (2006) Photosynthesis in the Archean Era. *Photosynthesis Research* 88: 109-127.

Pentecost, A., and Riding, R. (1986) Calcification in Cynobacteria. In: *Biomineralization in Lower Plants and Animals*, edited B.S.C Leadbeater and R. Riding, Springer, Netherlands 30: 73-90.

Rasband, W.S. (2014) ImageJ, U. S. National Institutes of Health, Bethesda, Maryland, USA,. Availaible online at: http://imagej.nih.gov/ij/.

Riding, R. (1991) Classification of Microbial Carboantes. In: *Calcareous Algae and Stromatolite,* edited by Riding, Spring-Verlag, Berlin, pp 21-51.

Riding, R. (2000) Microbial Carbonates: The Geological Record of Calcified Bacterial? Algal Mats and Biofilms. *Sedimentology* 47: 179-214.

Riding, R. (2006) Microbial Carbonates Abundance Compared with Fluctuations in Metazoan Diversity over Geologic Time. *Sedimentary Geology* 185: 229-238.

Riding, R. (2011) Microbialites, Stromatolite, and Thromobolites. In: *Encyclopedia of Geobiology*. *Encyclopedia of Earth Science Series*, edited by Reitner and V. Theil, Spring-Verlag, Berlin, pp. 635-654.

Simonson, B., and Carney, K. (1999) Roll-Up Structures: Evidence of in situ Microbial Mats Archean Deep Environments. *Palaios* 14: 13-24.

Sumner, D. (1997) Late Archean Calcite- Microbe Interactions: Two Morphologically Distinct Microbial Communitites That Affects Calcite Nucleation Differently. *Palaios* 12: 302-318.

Tice, M.M., and Lowe, D.R. (2004) Photosynthetic Microbial Mats in the 3,416-Myr-Old Ocean. *Nature* 43: 549-552.

Tice, M.M., Thornton, D.C.O., Pope, M.C., Olszewski, and T.D., Gong, J. (2011) Archean Microbial Mat Communities. *Annual Review of Earth and Planetary Sciences* 39: 297-319.

Trichet, J.B., and Defarge, C. (1995) Non-Biologically Supported Organomineralization, *Bull. Inst. Oceanogr. Monaco, Num. Spec.* 14: 203-236.

von Brunn, V., and Mason, T. (1977) Siliciclastic-Carbonate Tidal Deposits from the 300 M.Y. Pongola Supergroup, South Africa. *Sedimentary Geology* 18: 245-255.

Wade, L., Hodyss, R., Allwood, A., Gao, N., and Kozaczek, K. (2013) Micro-XRF for in situ Geological Exploration of Other Planets: X-Ray Fluorescence Instruments Are Used for Non-Destructive Testing, Sorting of Recyled Materials, and Hazardous Waste Detection, July NASA Tech Briefs, p. 23.

Webster, G. (2014) Jet Propulsion Laboratory, California Institute of Technology, Mars 2020 Rover's PIXL to Focus X- Rays on Tiny Targets [Press Release]. Available online at: http://www.jpl.nasa.gov/news/news.php?release=2014-253.

Weiner, S., and Dove, P.M. (2003) An Overview of Biomineralization and the Problem of the Vital Effect. In: *Biomineralization. Reviews in Mineralogy & Geochemistry,* edited by Dove, P.M., Weiner, S., De Yoreo, J.J., Mineralogical Society of America, Washington, D.C., pp. 1–29.

Zeng, Z., and Tice, M.M. (2014) Promotion and Nucleation of Carbonate Precipitation During Microbial Iron Reduction. *Geobiology* 12: 362-371.